Chapter 2

A Solar Adaptive Optics System

Ren Deqing and Zhu Yongtian

Additional information is available at the end of the chapter

http://dx.doi.org/10.5772/ 52834

1. Introduction

Solar activities are dominated by magnetic fields, which are arranged in small structure. The structure and evolution of small-size magnetic fields are the key component in a unified understanding of solar activities [1]. As such, a major application of a large solar telescope is for high-sensitivity observations of solar magnetic fields. The observation of solar dynamics of small-scale magnetic fields requires un-compromised high resolution, high magnetic field sensitivity, and high temporal resolution [2, 3]. The two important scales that determine the structuring of the solar atmosphere are the pressure scale height and the photon mean free path, which are of on the order 70 km or 0.1″. Recently, structures as small as a few tens of kilometers on the solar surface corresponding to a few tens of milli-arcseconds on the sky have been predicted by sophisticated MHD models of the solar atmosphere [4-7]. For a ground-based telescope, however, the atmospheric turbulence will seriously degrade the actual performance for high-resolution imaging, and an adaptive optics (AO) system is needed to recover the theoretical diffraction-limited angular resolution in real-time scale [8].

Current major solar telescopes have been equipped with dedicated AO systems that adopt different techniques for real-time wave-front sensing and image signal processing [9]:

1. The AO system with the 0.76-meter Dunn solar telescope uses Digital Signal Processors (DSPs) for the real-time signal processing [10]. DSPs are superb for fast calculation for digital image processing. However it is time-consuming for the DSP programming, and it lacks flexibility.

2. The 0.7-m Vacuum Tower Telescope at Teide Observatory uses multiple Processors (CPUs) on workstation computers and low-level programming language such as C++ for AO programming [11, 12].

The performance of the AO systems with multi-CPUs is close to those with DSPs. However, the low-level C++ programming is also time-consuming. Recent CPU developments indicate that multi-core technique is superior over that of the multi-CPU in view of the calculation speed and power consuming. A detailed review of solar adaptive optics was discussed by Rimmele and Marino [13].

Due to the rapid development of multi-core personal computers and the powerful parallelism of the LabVIEW software, we proposed a novel solar AO system that is based on today's multi-core CPUs and "high-level" LabVIEW programing [14]. The Portable Solar Adaptive Optics (PSAO) system at California State University Northridge (CSUN) is designed to deliver diffraction-limited imaging with 1~2-m class telescopes which will cover the largest solar telescope currently operational. This AO is optimized for a small physical size, so that we can carry it to any available solar telescope as a visiting instrument for scientific observations. We use personal computers with Intel i7 multi-core CPUs for the AO real-time control, and use LabVIEW software for AO programming. LabVIEW, developed by the National Instruments (NI), is based on block diagram programming, which makes it inherently supporting multi-core or multi-thread calculation in parallel. LabVIEW also includes a large number of high-quality existing functions for mathematical operations and image processing, which makes the AO programing extremely efficient and is suitable for the real-time AO programming.

Since 2009, we have built and continually updated our PSAO system in our laboratory [15]. We have initially tested the PSAO with the 0.6-m solar telescope at San Fernando Observatory (SFO) as well as the 1.6-m McMath-Pierce telescope (McMP). In this paper, we will present recent results in the development of the PSAP in the laboratory and the on-site trial observations.

2. Design philosophy

2.1. Optical Design

The PSAO must be able to work with any solar telescopes with different aperture size and focal ratios, although it was initially developed for testing with the 0.6-meter vacuum solar telescope located at the San Fernando Observatory, CSUN. For such an application, the PSAO optics consists of two individual parts. The first part is the fore-optics, while the second part is the main AO optics. The PSAO optics layout is shown in Figure 1. The fore-optics consists of L1, M1, L2 and M2, while the main AO optic consists of the remaining optical components. Where, L1 and L2 are two lenses and M1 and M2 are two fold mirrors. All the optical components are off-the-self parts. The function of the fore-optics is to convert a telescope's focal ratio to f/54, and create an exit pupil at infinite distance. i.e. create a telecentric image at f/54: in Figure 1, the telescope focal plane image IM0 is first collimated by lens L1, which forms a pupil image on the fold mirror M1. The pupil image is located one focal length distance from lens L2. In such a way, lens L2 forms a solar image at IM1 with the exit pupil at infinite. By adjust the focal length ratio between L1 and L2, one can convert the tele-

scope image IM0 to a telecentric image of f/54 at the IM1; the main AO optics is fixed even with different telescopes, except that the wave-front sensor lenslet array (L6 in Figure. 1) can be chosen from a set of lenslet arrays for different telescopes and seeing conditions. In this way, we only need to adjust the fore-optics without any change for the main AO optics, which makes the PSAO suitable with any solar telescope. For example, the 1.5-m McMP telescope, located at the Kitt Peak National Solar Observatory (NSO), has a focal ratio of f/54 at the focal plane. When working with the McMP, both lenses L1 and L2 are identical and have a focal length of 250mm. As shown in the Figure 1, we use two lenses L1 and L2 as the fore-optics which is of a typical telecentric optics design. The whole AO optics uses several flat fold mirrors (M1, M2, M3, M4) to fold the optical path and reduce the overall physical size. The fold mirror M1 in the fore-optics also serves as a tip-tilt mirror (TTM). The output focal plane image after the fore-optics (L2) is collimated by the lens L3, which creates a pupil image with a size of ~ 4.4-mm on the deformable mirror (DM). Please note that the fold mirror M4 also serves as the DM. After the DM, the beam is split as several parts by two beam splitters B1 and B2, which are used for DM wave-front sensing, tip-tilt sensing and focal plane imaging, respectively. Currently, our AO system has its individual optical channels for DM wave-front as well as tip-tilt sensing, respectively. The DM wave-front sensor (WFS) consists of lenses L4, L5, a lenslet array L6 (for clarity, only one lenslet is shown) and a WFS camera, while the tip-tilt sensor (TTS) consists of the lens L8 and the tip-tilt camera only.

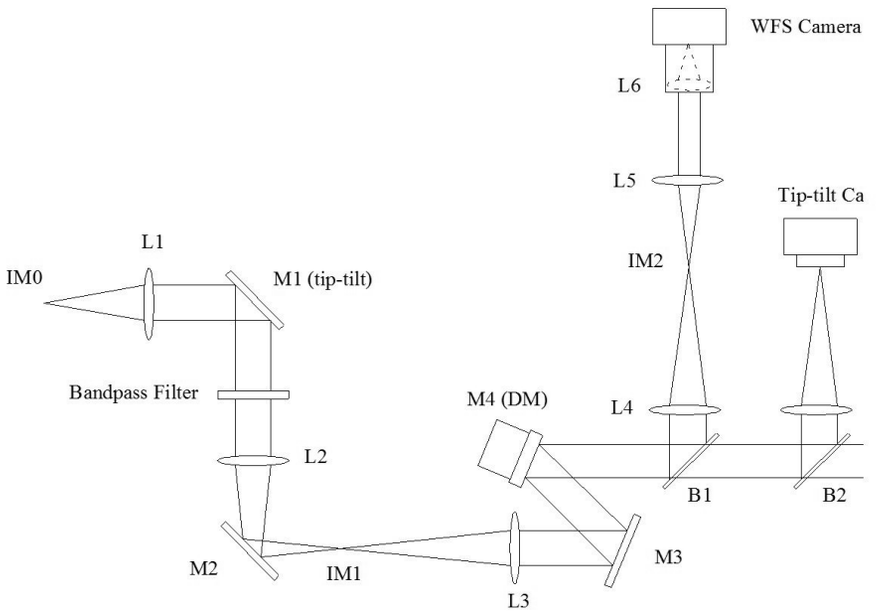

Figure 1. The optical layout of the PSAO.

For the DM WFS channel, lens L4 forms a telecentric solar image IM2, which is collimated subsequently by lens L5. A pupil image is formed one focal length distance behind lens L5, where the lenslet array L6 is located to sample the pupil image for proper wave-front sensing. This is a typical configuration of a Shack-Hartmann wave-front sensor, except that the field of view (FOV) formed by each lenslet must have a suitable size for wave-front sensing

with a two-dimensional solar structure. A typical field size for solar wave-front sensing is in a range of 15″ ~ 20″, which is a compromise between the wave-front sensing speed and the sensing accuracy. The TTS is very simple. A lens L8, which is a zoom lens, is used to form a solar image directly on the tip-tilt camera for the calculation of the overall image movement. The corrected image is fed directly to the science camera via the lens L9, which is changeable for different image scales with different telescopes.

The WFS - DM and TTS - TTM channels are controlled by two high performance personal computers to form two individual correction loops, respectively; one is for the DM wave-front correction and the other is for the tip-tilt correction. The DM and TTM are both conjugated on the telescope pupil, which eliminates the pupil wander problem and ensures the AO correction extremely stable. A field stop is placed on the telescope focal plane IM0 or on the solar image plane IM1. An adjustable field stop is also located on the solar image plane IM2 to limit the field size for wave-front sensing. The lenslet array is integrated with the WFS camera directly via the camera's C mount, and can be replaced for different focal lengths, which makes the PSAO suitable for different telescopes and seeing conditions.

A band-pass filter is located just before lens L2. The filter has a band-pass width of ~ 100 nm, which will limit the light energy on the small DM. This is not a problem for solar scientific observations, which only need to work on narrow band in most situations. In fact, a filter wheel can be used for the observations at any band. The size of the AO field of view is controlled by the aperture size of a field stop located on the IM0 (or IM1), which limits the AO field of view as 60″x60″. The field of view for the TTS is also set the same as that of the AO field of view, and is sampled by 60x60 pixels of a "region of interest" of the tip-tilt camera, which results in a sampling scale of 1″/pixel. The primary optical specifications are listed in Table 1.

AO FOV	TTS FOV	WFS FOV	Wavelength range
60″x60″	60″x60″	8″x8″ ~ 30″x30″	0.6 ~ 1.5μm

Table 1. PSAO Optical Specifications.

The use of an individual DM wave-front sensor as well as a tip-tilt sensor has some benefits. In addition to avoid the pupil wander for the wave-front sensing, which will deliver a super stable AO system at different seeing conditions, it will allow the use of small field of view for wave-front sensing at good seeing condition, which can further improve the wave-front sensing sensitivity or accuracy. Since the PSAO has its individual DM wave-front and tip-tilt sensors, the TTS can be used to measure the overall wave-front movement in the large 60″x60″ FOV. As the wave-front tip-tilt component is corrected by the tip-tilt mirror, the DM WFS can use a small FOV, such as 8″x8″, for accurate wave-front sensing. Since each WFS lenslet sub-aperture is sampled by 30x30 pixels in our WFS, a 8″x8″ FOV corresponds to a WFS sampling scale of 0.27″ /pixel, compared to the 1.0″ /pixel sampling scale for a 30″x30″ WFS FOV that may be used in poor seeing conditions. This can significantly improve the wave-front sensing accuracy and thus deliver a better AO performance.

2.2. Wave-Front Sensing

Solar wave-front sensing uses a Shark-Hartmann wave-front sensor. The wave-front gradient or slope vector at each sub-aperture of the lenslet array is solved by the cross-correlation calculation of a two-dimensional pattern over a field of view. The correlation function C(x,y) of a sub-aperture S(x,y) and a reference pattern R(x,y) can be calculated over the two-dimensional sub-aperture as

$$C(x,y) = FFT^{-1}[FFT(S)\cdot(FFT(R))^{*}] \tag{1}$$

the asterisk denotes the complex conjugate. FFT and FFT^{-1} represent Fourier and inverse Fourier transfers, respectively. The resulting correlation function is "star-like" and can be treated like a star in the stellar WFS. The position of the maximum value of the correlation function corresponds to a slope vector where the reference pattern of R(x,y) best matches the sub-aperture pattern of S(x,y). The calculations of the Fourier and inverse Fourier transfers for the so-called pattern match are time consumed, which makes the high-speed AO correction challenging.

If wave-front phase ϕ is described by the Zernike polynomial expansion as

$$\varphi = \sum_{k=1}^{K} a_k Z_k(x,y) \tag{2}$$

From equation 2, the slope vector s of the WFS and mode coefficient vector a are associated as

$$\boldsymbol{s}=[B]\boldsymbol{a} \tag{3}$$

where,

$$S = \left(\frac{\partial\varphi}{\partial x}\Big|_1 \ldots\ldots \frac{\partial\varphi}{\partial x}\Big|_M \quad \frac{\partial\varphi}{\partial y}\Big|_1 \ldots\ldots \frac{\partial\varphi}{\partial y}\Big|_M\right)^T \tag{4}$$

$$\boldsymbol{a} = (a_1 \quad a_2 \ldots\ldots a_k)^T \tag{5}$$

while the matrix [B] is

$$[B]=\begin{pmatrix} \left.\frac{\partial Z_1(x,y}{\partial x}\right|_1 & \left.\frac{\partial Z_2(x,y}{\partial x}\right|_1 \cdots \left.\frac{\partial Z_K(x,y}{\partial x}\right|_1 \\ \vdots & \\ \left.\frac{\partial Z_1(x,y}{\partial x}\right|_M & \left.\frac{\partial Z_2(x,y)}{\partial x}\right|_M \cdots \left.\frac{\partial Z_1(x,y}{\partial x}\right|_M \\ \left.\frac{\partial Z_1(x,y}{\partial y}\right|_1 & \left.\frac{\partial Z_2(x,y}{\partial y}\right|_1 \cdots \left.\frac{\partial Z_K(x,y}{\partial y}\right|_1 \\ \vdots & \\ \left.\frac{\partial Z_1(x,y}{\partial y}\right|_M & \left.\frac{\partial Z_2(x,y)}{\partial y}\right|_M \cdots \left.\frac{\partial Z_1(x,y}{\partial y}\right|_M \end{pmatrix} \tag{6}$$

Here, M is the number of WFS sub-apertures. K is the number of Zernike modes. The mode coefficient vector is found by finding the pseudo-inverse of [B], which is solved by using the singular value decomposition (SVD) as,

$$[B]=UDV^T \tag{7}$$

and,

$$[B]^{-1}=VD^{-1}U^T \tag{8}$$

Once the DM's influence function is known, the measured wave-front is used to find the DM' signals (i.e. voltages) that are required to correct the wave-front error. The Zernike polynomials act as a low-band pass filter, which is used to measure and control the actual wave-front error up to the mode number K. The choice of actual mode number that an AO system can correct should consider the system's stability, which can be determined by the condition number as discussed by Kasper et al. [16].

2.3. Electrics and Programming

All the PSAO's hardware is based on off-the-shelf commercial components, which makes a low cost system possible. The performance of our AO system can continue to improve once better components are available on the market. The current AO WFS loop uses a computer equipped with a first-generation Intel i7 -990X CPU, which has 6 cores and 12 threads for parallel computation. This computer can be updated to a second-generation Intel i7 CPU that should deliver a better performance, or even updated to a computer with two recent Xeon CPUs that will have 16 cores and 32 threads in total, which is expected to be two times faster than the current system. The specifications of current hardware components are listed in the Table 2.

http://dx.doi.org/10.5772/ 52834

Hardware	Specifications
DM	140 actuators, 3.5μm stroke, 14-bit resolution, 4.4-mm clear aperture, 8000 Hz frame rate.
TTM	PI S-330.4SL, 5mrad stroke range, 0.25μrad resolution, 1600 Hz frame rate.
WFS & Tip-tilt Camera	1024x1024 pixels, 10.6μm pixel size, 150Hz frame rate at full resolution.
Image Grabbers	NI PCIe-1429 Camera-Link image grabber.
WFS lenslet arrays	0.3mm pitch, 4.7mm, 8.7mm, 18.8mm focal lengths.
Computer 1 (for WFS loop)	Intel Core i7-990X @ 3.47GHz, 8GB RAM.
Computer 2 (for TTS loop)	Intel Core i7-980X @ 3.33GHz, 4GB RAM.

Table 2. PSAO Hardware specifications.

The DM and TTM are two critical components for the AO system. We use the high-speed Multi-DM from Boston Micronmachines Corporation (BMC), which is a micro-electro-mechanical-systems (MEMS) deformable mirror and has 140 actuators (in a 12x12 array without 4 corners) with 3.5μm stroke and can deliver a frame rate up to 8000 Hz. The DM has a clear aperture of 4.4 mm only. Although this allows for a small beam size and makes the whole AO system smaller in physical size, a DM with a clear aperture on the order of 8~10mm will be preferred for our AO system, which will not significantly increase the physical size and will be more robust to the alignment error between the DM and the WFS, such as the error introduced by the vibration from where the AO is located. If the DM had an 8-mm clear aperture, for example, the focal ratio at IM1 in Figure 1 could be f/27, instead of f/54, and in this case lens L3 will has the same focal length with that for the 4.4-mm DM, and thus will not increase the overall AO physical size. The TTM is a flat mirror mounted on a S-330.4SL piezo-tilt platform from Physik Instrumente (PI), which has 5-mrad stroke and can deliver an actual frame rate of 700 Hz only with the digital USB input port, although the datasheet claims that it has a unloaded resonant frequency of 3.3 kHz, and a resonant frequency of 1.6 kHz loaded with a 25 x 8 mm glass mirror. The strokes of our DM and TTM are both sufficient for the AO requirements. In theory, the WFS can simultaneously measure tip-tilt and high-order wave-front errors so that the DM and TTM can be controlled by one computer only. However the current TTM maximum frequency is too slower, comparing to that of the DM, which will reduce the overall AO correction speed, if both were controlled by a single closed-loop. In order to keeping the DM correction fast, we split the DM wave-front and tip-tilt corrections as two individual close-loops, and use two computers to control the DM and TTM, separately.

Both the DM wave-front sensor and the tip-tilt sensor adopt a high-speed MV-D1024E-CL160 camera made by Photonfocus, respectively. The camera transfers image data via the base camera-link interface at a speed of 255MB/s. The output data from each camera is acquired by a high-performance NI PCIe-1429 Camera-Link image grabber connected to the

associated controlling computer via a PCIe slot. We chose the NI image grabbers for both WFS and TTS cameras, since many existing LabVIEW standard functions for image acquisition are supported by this grabber. The NI PCIe-1429 image grabber supports full, medium, and base camera-link interfaces. The camera can achieve a rate up to 150 frames/second at full-resolution with 1024x1024 pixels. Since we only use a small region of interest with ~ 300x300 pixels for wave-front sensing, the acquisition speed can achieve 1800 frames/s. For the TTS, we only use 60x60 pixels. In a future update, we schedule to use a full camera-link camera, which should be able to deliver an image data acquisition at a speed of ~800 MB/s.

The most time-consuming part in the PSAO is the wave-front sensing and the calculation of control signals for the DM wave-front correction, which must be executed with a high performance computer. The computer used for DM wave-front correction loop has an Intel Core i7-990X CPU with 6 cores, at a clock frequency of 3.47GHz. The computer used for the tip-tilt correction loop has an Intel Core i7-980X CPU with 6 cores, at a clock frequency of 3.33GHz. Here we choose the computer with a single CPU with multiple cores other than the multiple CPUs, since these multiple CPUs are mainly optimized for large data handling such as for internet servers, and are not optimized for real-time calculation and control. This problem will be solved by the latest Intel Xeon E5-2600 series processors which adopt the same architecture with the Core i7 processor, and have up to 8 cores per CPU. A computer equipped with 2 Intel Xeon E5-2687W CPUs for the DM wave-front correction loop is expected to increase the closed-loop bandwidth of our AO system better than 100 Hz, which will be on the state-of-the-art of the current solar AO systems.

Our AO software is written in LabVIEW codes. LabVIEW's Graphical programs inherently contain information about which parts of the code should execute in parallel. Parallelism is important in AO programing because it can unlock performance gains relative to purely sequential programs, due to recent changes in computer processor designs, in which CPUs are moved to multi-cores. LabVIEW also has a large number of standard functions for image processing, mathematical operations and hardware control. These high-quality functions are optimized for high-speed calculation as well as real-time control. For example, the standard function of pattern match in LabVIEW is about 6 ~ 9 times faster than the conventional cross-correlation algorithm. To fully take advantage of the power of today's multi-core CPU and high-quality LabVIEW's graphic programming, we use LabVIEW's parallel programming, which makes rapid development of a high-performance AO system possible. LabVIEW has greater flexibility and capability for real-time hardware system control than other general-purpose programming languages. LabVIEW programming is performed by wiring together graphical icons on a diagram, in which each icon is a built-in function. This makes programming extremely easy and efficient. In addition, dataflow languages like LabVIEW allow for automatic parallelization. Graphical programs inherently contain information about which parts of the code should execute in parallel. In the future, our system can also be easily updated to a full field-programmable gate array (FPGA) system by using NI's PXI system that is fully supported by NI's LabVIEW parallel programming, which may further increase the AO correction speed. Historically, FPGA programming was the province of only a specially trained expert with a deep understanding of digital hardware design languag-

es. LabVIEW's FPGA programming makes it possible for engineers without FPGA expertise to use it, and makes the software development efficient.

The AO software is composed of two parts. The first part is for the AO calibration, which automatically searches for all effective WFS sub-apertures, calculates DM influence function, and record all the calibration data; the second part is for AO real-time correction, which first reads the calibration data and then performs wave-front correction in real-time. Due to the intrinsic support for parallel processing, LabVIEW automatically assigns the calculation tasks as multiple threads for each core, so that the program can be run in parallel, which greatly increases the running speed for the AO wave-front sensing and correction.

2.4. Tip-Tilt and Deformable Mirror Requirements

Since the atmospheric turbulence is corrected by the tip-tilt and deformable mirrors, the strokes provided by the tip-tilt or deformable mirror must be sufficiently large, so that the wave-front errors can be effectively corrected. Here, we use the 1.6-meter McMP as an example to calculate the tip-tilt and DM requirements. The total minimum stroke required for the tip-tilt mirror is given by [17]

$$Stroke_{\min} = 1.25\frac{D}{D_{tilt}}\sqrt{0.184(\frac{D}{r_0})^{5/3}(\frac{\lambda}{D})^2} \tag{9}$$

where, D is the telescope aperture size and is equal to 1.6 meters for the McMP. D_{tilt} is the diameter of the telescope aperture de-magnified on the tilt mirror. Assume that the telescope aperture is de-magnified as ~5.0 mm on the tip-tilt mirror, D_{tilt} is equal to 5.0 mm. At 1.25-μm wavelength, r_0 is equal to 150 mm (see next subsection). This results in a minimum stroke of 0.001 radians. The tip-tilt mirror will be mounted on a S-330.4SL piezo-tilt platform that can provide a maximum tilt of 0.005 radians that is larger than the minimum stroke requirement.

Similarly, the required stroke for the deformable mirror is calculated as [17]

$$Stroke\ \ (waves) = 2.5\sqrt{0.00357(\frac{D}{r_0})^{5/3}} \tag{10}$$

This results in a required stroke of 1.08 waves at 1.25-μm wavelength. The deformable mirror from BMC can provide a maximum stroke of 3.5 μm that is larger than the required stroke. BMC's deformable mirrors are being used for astronomic adaptive optics systems, where large amount of actuators or a compact design is required. For example, the "Extreme Adaptive Optics" will use a BMC deformable mirror for the 8-meter Gemini telescope, where a deformable mirror with 4096 actuators is required [18]. The high-speed MBC Multi-DM was also used for stellar adaptive optics with a small physical size [19]. The precision and stability of the BMC's deformable mirror have been proved by our past experiences.

2.5. Performance Estimation

As an example, the AO performance estimation will only focus on the Kitt Peak 1.6-meter McMP that has a large aperture size. The estimated performance should be better for other telescope with a smaller aperture size or a site with a better seeing condition. The Fried parameter r_0 is equal to ~ 5 cm at 0.5 μm for the daytime median seeing conditions at Kitt Peak, which is available almost every week for a clear sky. The seeingr_0 is scalable with wavelength as $r_0 \propto \lambda^{\frac{6}{5}}$ for Kolmogorov turbulence, and it reaches 70 mm and 150 mm at the 0.65 μm and 1.25 μm wavelengths, respectively.

A DM surface with a finite actuator number cannot exactly match the wave-front patterns of the atmospheric turbulence. For an atmospheric wave-front with Kolmogorov spectrum, the fitting error variance of a DM with finite actuator number is derived by Hudgin [20] and is given as

$$\sigma_{fit}^2 = \kappa(r_s / r_0)^{5/3} \tag{11}$$

where r_s and r_0 are the spaces between two actuators and the Fried parameter, respectively. κ is the fitting parameter. Since there are 12 actuators across the DM aperture that is conjugated onto the 1.0-meter effective telescope aperture (see Section 4) although McMP has a 1.6-meter aperture,r_s is equal to 83 mm. An extensive analysis of the fitting error showed that κ=0.349 was applicable for many influence functions that are not constrained at the edge [21]. Therefore, the fitting error variance $\sigma_{fit}^2$is 0.46 radians^2 and 0.25 radians^2 at the 0.65 μm and 1.25 μm wavelengths, respectively.

The temporal error of the wave-front correction is determined by the Greenwood frequency and the bandwidth of the AO system. The Greenwood frequency can be calculated as $0.43v/r_0$ [22], where $v$is the average wind speed. At McMP, when wind speed reaches 20 m/s, the telescope will be closed and observations will not take place. We assume that the AO system will operate with an average wind speed of 8.0 m/s. This results in a Greenwood frequency of 49 Hz and 23 Hz at the 0.65 μm and 1.25 μm wavelengths, respectively. The wave-front variance due to the temporal error of the correction can be calculated as $\sigma_{tem}^2=(f_G / f_{BW})^{5/3}$, where f_G is the Greenwood frequency and f_{BW} is the bandwidth of the AO system. Since the AO closed-loop bandwidth is 80 Hz, the temporal wave-front variance $\sigma_{tem}^2$is 0.44 radian^2 and 0.13 radian^2 at the 0.65 μm and 1.25 μm wavelengths, respectively.

Read out noise is not a problem for solar wave-front sensing since plenty of photons are available for the wave-front sensing [10]. The corrected wave-front variance is the sum of all the error contributors. If only the fitting and temporal errors are considered, the wave-front variance can be calculated approximately as$\sigma^2 \approx \sigma_{fit}^2 + \sigma_{tem}^2$. This results in a wave-front variance of 0.90 radian^2 and 0.38 radian^2 at the 0.65 μm and 1.25 μm wavelengths, respectively. The overall performance of an AO system can be evaluated in terms of the Strehl ratio,

which defines the peak of the actual point spread function normalized to the peak of the diffraction-limited point spread function. The Strehl ratio is calculated as $S = e^{-\sigma^2}$. At 0.65 μm, the AO system is expected to achieve a Strehl ratio of ~ 0.41; at 1.25 μm, it will deliver a Strehl ratio of ~ 0.68, and should deliver a better correction at longer wavelengths.

3. Recent laboratory tests

The PSAO was first built in CSUN laboratory in 2009, with an OKO 37-actuator DM for software development and test purpose. In 2010, the DM was upgraded with the current BMC 140-actuator model. A cross target illuminated by a white-light fiber bundle is used for the 2-dimensional object test. A 32-actuator DM from Edmund Optics is used to generate a real-time wave-front aberration at a desired frequency, which is subsequently fed into the AO system, so that the AO performance can be evaluated in real-time. The whole optics of PSAO is built on a 900mm x 600mm optical breadboard as shown in the Figure 5, and can be easily carried to any solar observatory.

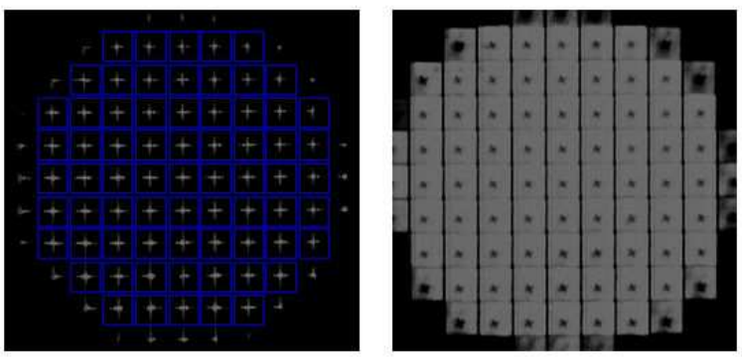

Figure 2. Graphic WFS interfaces for AO calibration with a point source (left) and for real-time correction with a cross target (right).

The AO software consists of two parts. The first part is used for the AO calibration, while the second part is the code for AO real-time correction. In principle, the calibration only needs to be done once a time, provided that the hardware has not been realigned. In the calibration, a single-mode fiber is served as a point source. Any possible incoming wave-front error will be filtered out by the single-mode fiber, and only the fundamental mode can propagate through the fiber. The output wave-front can be viewed as a perfect wave for the calibration. In the calibration, the fiber is switched into the optical path on the telescope focal plane just before the lens L1 (see Figure 1). In AO real-time correction, the fiber is switched out the optical path, and an extended target (a cross herein), including the wave-front error generated by the 32-element Edmund Optics DM, is allowed to input into the AO for testing. A lenslet array with 8.7-mm focal length is used for the WFS. Figure 2 shows the WFS interfaces in the AO calibration with a point source (Figure 2 left) and in real-time correction with a cross target (Figure 2 right): there are 69 effective WFS sub-apertures arranged in the

9x9-lenslet grid configuration and wave-front correction up to 65 modes of Zernike polynomials can be chosen. Please note that in this test, there is no central obstruction on the pupil, although our software can be used with a telescope with central obstruction.

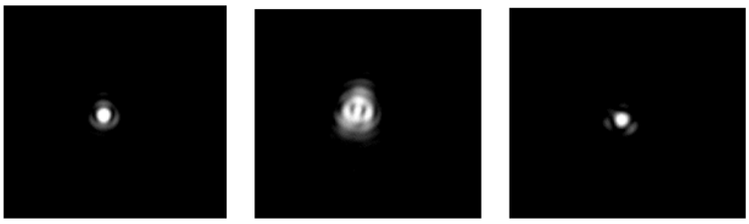

Figure 3. Point-source images: original image without aberration applied (left), with aberration applied and AO off (center), with aberration applied and AO on (right). 9x9 lenslets (without those on the four corners) are used for wave-front sensing, and 25 Zernike modes are corrected.

The PSAO had achieved excellent corrections in the test with a point source target. Figure 3 shows the original point-source image (left) without aberration applied, as well as the AO-off (center) and AO-on (right) images with the aberration applied, respectively. In this test, the wave-front error was introduced by the 32-actuator Edmund Optics DM in real-time, in which the wave-front is variable as a sinusoidal function with a frequency up to 80Hz. The central image of the distorted point-spread function shows that the wave-front error applied is significantly large, while the right image clearly demonstrates that the AO system can recover the diffraction-limited image. The AO system demonstrated good results in different situations:

1. the amplitude of the applied wave-front error is less or equal to the AO DM's maximum stroke (see Figure 3 and Figure 4). In this situation, the AO system can almost completely correct the wave-front and deliver the same image quality as that there is no wave-front error (i.e. the wave-front error is not been applied);

2. wave-front error with amplitude larger than the AO DM's maximum stroke is applied, which simulates the bad seeing condition on a site. The AO system can still compensate part of the wave-front error, which is consistent to the DM's maximum stroke. Therefore, the image quality can still be improved.

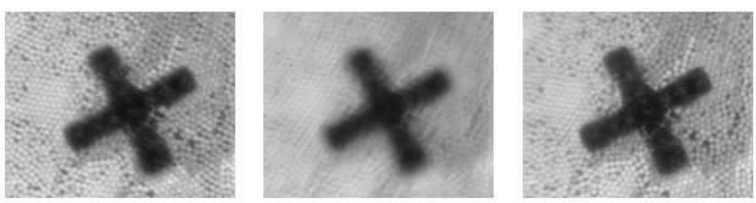

Figure 4. Cross-target images: original image without aberration applied (left), with aberration applied and AO off (center), with aberration applied and AO on (right). 9x9 lenslets (without those on the four corners) are used for wave-front sensing, and 25 Zernike modes are corrected.

The AO system was also tested with a 2-dimensional extended target with the same procedure for the point-source target. In this test, a cross was printed on a transmission film and was used as a 2-dimensional target. A fiber bundle light source located immediately behind the cross target was used to illuminate it, so that the image of the fibers was almost overlapped on the cross target, except for a slight defocus between them. Figure 4 shows the original cross-target image (left) without aberration applied, as well as the AO-off (center) and AO-on (right) images with the aberration applied, respectively. Please note that the image of the cross target and background small fibers is seriously blurred by the wave-front error applied (center image). Compared the left and right images, however, it is clear that the AO recovers the original image perfectly, indicating that the AO's performance is excellent. In fact, our AO system can recover the original wave-front that is associated with the original image with accuracy up to 1/1000 wave-length in the visible [23].

4. Recent on-site observations

The PSAO's small size makes it can be easily brought to any observatory for science observations. Since 2010, we have carried out observations at two different sites. To demonstrate the AO's feasibility, an initial on-site observation was conducted by using the 0.61-m solar telescope at the San Fernando Observatory, California State University Northridge. This solar telescope is a three-aspheric mirror system with a central obstruction area of 14%, and a focal ratio of f/20. Because of the poor seeing conditions at the San Fernando Observatory, WFS with 9x9 sub-apertures (exception those in regions of the four-corners and the central obstruction) was used. The best observational results were acquired in October 2011. Using a sunspot as a target, the AO system was able to lock on the sunspot for wave-front sensing and provides high-resolution images at the wavelength of 0.75 μm [24], which indicates that our PSAO is able to provide wave-front correction at a site with a poor seeing condition.

After the successful observations on the San Fernando Observatory, we continued to test this system with the 1.6-m McMP. The McMP is located at the Kitt Peak, and is operated by the National Solar Observatory. It is one of the largest solar telescopes and is accessible to the solar community around the world. The medium seeing at the Kitt Peak is better than that at the SFO, but is still poor with a Fried parameter of ~ 5 cm at median seeing condition. The poor seeing condition at the Kitt Peak is a great challenge for an adaptive optics system. There are no AO available for routine observations with the McMP, although a prototype with 36-actuator DM was developed many years ago [25]. McMP is an off-axis telescope without central obstruction. The solar image is formed on a rotational station at f/54, where our PSAO can be conveniently placed for observations. Figure 5 shows the PSAO loaded on the McMP rotation station for an observation, in which the small size of the AO system is clearly referred. The non-common optical path error between the WFS and the science camera, which the WFS cannot measure, was calibrated by an approach we proposed recently [23].

During the latest observations in May 2012, the PSAO delivered excellent performance in the visible with the McMP. Solar images were captured at 0.6-μm visible wavelength. Figure 6

shows the typical images of Sunspot 1492 with the AO off and AO on respectively, on the May 28 run. For the AO off images, the AO still provides the tip-tilt correction, so that the overall image movement is corrected. Compared with the poor image quality when the AO is switched off, the AO system provides significant improvement for the image quality when the AO is switched on, which demonstrates the power of the AO correction: the granules around the sunspot can be clearly seen with the AO correction, while they are totally blurred and disappeared without the correction. The AO off image clearly shows how poor the seeing condition was during our observation run. In the observation, only 7x7 sub-apertures were used for the WFS, and only 1.0-meter of the McMP aperture was used for imaging, because a small area on the edge of the telescope primary mirror was damaged and the telescope heliostat was tilted at a large angle during the observation, which delivered an useful circle aperture on the order of 1.0-meter in diameter. Each sub-aperture was sampled by 30x30 pixels of the WFS camera. The AO delivered an open-loop bandwidth of 800 Hz, which corresponds to a closed-loop bandwidth of ~ 80 Hz. The improvement of image performance with the AO correction was significant. This was the first time demonstration that an AO system can be effectively used for high-resolution imaging in the visible with the McMP.

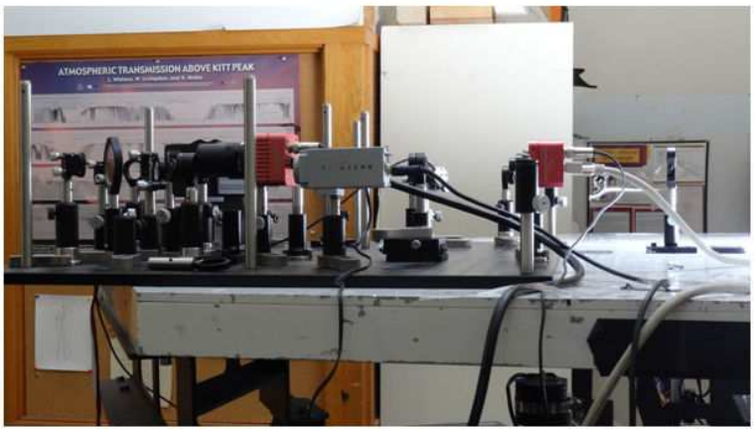

Figure 5. PSAO setup (the black breadboard) on the McMP rotation station. The two red cameras are used for WFS and TTS, while the grey one is the science camera.

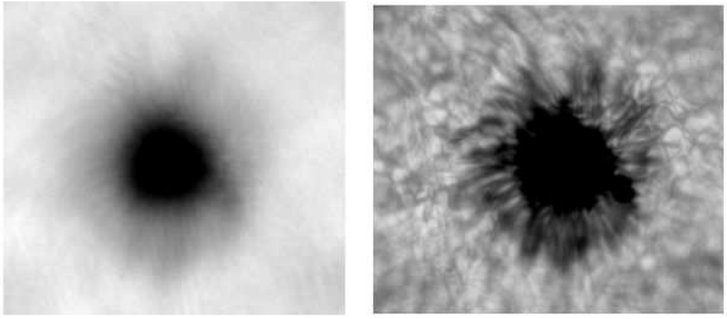

Figure 6. Sunspot 1492 image captured on the McMP with the AO off (left) and AO on (right).

http://dx.doi.org/10.5772/ 52834

Because of the poor seeing conditions at the Kitt Peak, only large sunspots can be used for wave-front sensing. Other small fine structures such as solar granules and pores are seriously distorted by the strong atmospheric turbulence and cannot be resolved by the WFS, which prevent accurate wave-front sensing by using a small WFS field of view. In this observation, lenslet array with 8.7-mm focal length was used for the WFS. The WFS field of view is 30″x30″ and is sampled by 30x30 pixels, which results in a sampling scale of 1.0″/pixels. Although the wave-front sensing of the AO software can execute with sub-pixel accuracy, such an improvement is very limited because of a number of reasons, such as the distortions of the sunspot images in each sub-aperture as well as the low contrast image resulted from the strong wave-front error. Better performance should be achievable with telescopes with good seeing conditions, where small fine solar structures can be used for accurate wave-front sensing.

4. Conclusions

We have fully demonstrated the feasibility of a portable AO system, both in the laboratory and on-site observations. The system is able to provide a wave-front correction with different telescopes with the aperture size up to 1.6 meters. Our AO system features low cost, high-performance, and is compact. Combining the multi-core computer and LabVIEW parallel programming, the AO system is particularly flexible and can achieve good performance. The open-loop correction speed can achieve 800Hz with sub-pixel accuracy for wave-front sensing, for the 7x7 sub-aperture WFS when 25 modes of Zernike polynomials of the wave-front are corrected. It can further achieve 1100 Hz, if sub-pixel wave-front sensing accuracy is not required. Higher wave-front correction speed should be able to achieve by using more CPU cores with a computer. The commercial CPU market for personal computers is being evolved rapidly, with efforts focusing on multi-core CPUs. For example, two Eight-Core Intel Xeon E5-2687W CPUs can be installed in a computer, which will deliver 16 cores in total and each core can run at 3.1GHz clock frequency. In another approach, we are also developing LabVIEW based FPGA technique, which may dramatically increase the running speed of the AO system. The 12x12-actuator DM is also being updated to a 24x24-actuator DM that will have a clear aperture of 9.0 mm, and should deliver better performance. The PSAO is being upgraded accordingly, and we will report our progresses in the near future.

Acknowledgements

This work is supported by the National Science Foundation under the grant ATM-0841440, the National Natural Science Foundation of China (NSFC) (Grant 10873024 and 11003031), the National Astronomical Observatories' Special Fund for Astronomy-2009, as well as the Strategic Priority Research Program of the Chinese Academy of Sciences (Grant No. XDA04070600). We thank Dr. Xi Zhang for his contribution to this AO project, and we grate-

fully acknowledge the assistances from the staff at Kitt Peak National Solar Observatory during our observations with the McMP.

Author details

Ren Deqing[1,2,3*] and Zhu Yongtian[2,3]

*Address all correspondence to: ren.deqing@csun.edu

1 Physics & Astronomy Department, California State University Northridge, USA

2 National Astronomical Observatories/Nanjing Institute of Astronomical Optics & Technology, Chinese Academy of Sciences, China

3 Key Laboratory of Astronomical Optics & Technology, National Astronomical Observatories, Chinese Academy of Sciences, China

References

[1] Stenflo, Jan. Olof. (2004). Solar physics: Hidden magnetism. *Nature*, 430(6997), 304 -305.

[2] Paletou, F., & Aulanier, G. (2003). On the Need of High-Resolution Spectropolarimetric Observations of Prominences . *in Current Theoretical Models and Future High Resolution Solar Observations: Preparing for ATST, ASP Conference Series286, held March 2002 at NSO, Sunspot, New Mexico, USA, Alexei A. Pevtsov and Han Uitenbroek (eds.), (NSO, Sunspot, New Mexico, USA)*, 11-15.

[3] Lin, H. (2003). ATST near-IR spectropolarimeter. *Proc. SPIE*, 4853, 215-222.

[4] Cattaneo, F., Emonet, T., & Weiss, N. (2003). On the Interaction between Convection and Magnetic Fields. *ApJ*, 588, 1183-1198.

[5] Vögler, A., & Schüssler, M. (2007). A solar surface dynamo. *Astron. Astrophys*, 465, L43-L46.

[6] Nordlund, Å., Stein, R. F., & Asplund, M. (2009). Solar Surface Convection. *Living Rev.Solar Phys*, 6, 2.

[7] Nordlund, Å., & Stein, R. F. (2009). Accurate Radiation Hydrodynamics and MHD Modeling of 3-D Stellar Atmospheres. *in Recent Directions in Astrophysical Quantitative Spectroscopy and Radiation Hydrodynamics, Proceedings of the International Conference in Honor of Dimitri Mihalas for His Lifetime Scientific Contributions on the Occasion of His 70th Birthday, Boulder, Colorado, March 30- April 3, , (Eds.) Hubeny, I., Stone, J.M., Mac-*

Gregor, K., Werner, K., of AIP Conf.Proc.American Institute of Physics, Melville, NY, 1171, 242-259.

[8] Woger, F., von der Luhe, O., & Reardon, K. (2008). Speckle interferometry with adaptive optics corrected solar data. *Astron. Astrophys*, 488, 375-381.

[9] Rimmele, T. R. (2004). Recent advances in solar adaptive optics. *Proc.SPIE*, 5490, 34-46.

[10] Rimmele, T. R., Richards, K., Hegwer, S., Ren, D., Fletcher, S., & Gregory, S. (2003). Solar adaptive optics: A progress report. *Proc. SPIE*, 4839, 635-646.

[11] van der Luhe, O., Soltau, D., Berkefeld, T., & Schelenz, T. (2003). KAOS: Adaptive optics system for the Vacuum Tower Telescope at Teide Observatory . *Proc. SPIE*, 4853, 187-193.

[12] Berkefeld, T., et al. (2010). Adaptive optics development at the German solar telescopes. *Applied Optics*, 49(31), G155 -G166 .

[13] Rimmele, T. R., & Marino, J. (2011). "Solar Adaptive Optics". *Living Reviews in Solar Physics*, 8(2), 1 -92 .

[14] Ren, D., Penn, M., Wang, H., Chapman, G., & Plymate, C. (2009). A Portable Solar Adaptive Optics System. *Proc. of SPIE*, 74380-1.

[15] Ren, D., Penn, M., Plymate, C., Wang, H., Zhang, X., Dong, B., Brown, N., & Denio, A. (2010). A portable solar adaptive optics system: software and laboratory developments. *Proc. SPIE*, 77363-7.

[16] Kasper, K., et al. (2000). ALFA: adaptive optics for the CALAR ALTO Observatory optics, control systems, and performance. *Experience Astronomy*, 10, 49-73.

[17] Tyson, R. K. (2000). Introduction to adaptive optics. *SPIE Press, Washington, USA*.

[18] Macintosh, B., et al. (2006). The Gemini Planet Imager Proc. *SPIEL*, 6272-62720L.

[19] Morzinski, K., Johnson, L. C., Gavel, D. T., Grigsby, B., Dillon, D., Reinig, M., & Macintosh, B. A. (2010). Performance of MEMS-based visible-light adaptive optics at Lick Observatory: closed- and open-loop control . *Proc. SPIE*, 7736-77361O.

[20] Hudgin, R. H. (1977). Wave-front compensation error due to finite correction-element size,. *J. Opt. Am*, 67, 393-395.

[21] Tyson, R. K., Crawford, D. P., & Morgan, R. J. (1990). Adaptive optics system considerations for ground-to-space propagation. *Proc.SPIE*, 1221, 146-156.

[22] Tyson, R. K. (1998). Principles of Adaptive Optics 2th edition. *Academic Press*.

[23] Ren, D., Dong, B., Zhu, Y., & Damian, J. C. (2012). Correction of non-common path error for extreme adaptive optics. *PASP*, 124, 247-253.

[24] Ren, D., & Dong, B. (2012). Demonstration of portable solar adaptive optics system. *Optical Engineering*, 51, 101705 -4.

[25] Keller, C. U., Plymate, C., & Ammons, S. M. (2003). Low-cost solar adaptive optics in the infrared. *Proc. SPIE*, 4853, 351-359.

IntechOpen